Template-oriented synthesis of monodispersed SnS$_2$@SnO$_2$ hetero-nanoflowers for Cr(VI) photoreduction

Xi Zhang [a,b], Peng Zhang [a,b,*], Lijie Wang [a,b], Hongqing Gao [a,b], Jiangtao Zhao [a,b], Changhao Liang [d], Junhua Hu [a,b,**], Guosheng Shao [a,b,c]

[a] School of Materials Science and Engineering, Zhengzhou University, Zhengzhou 450001, People's Republic of China
[b] State Centre for International Cooperation on Designer Low-carbon and Environmental Materials (SCICDLCEM), Zhengzhou University, Zhengzhou 450001, Henan, People's Republic of China
[c] Institute for Renewable Energy and Environmental Technologies, University of Bolton, Bolton BL3 5AB, UK
[d] Key Laboratory of Materials Physics and Anhui Key Laboratory of Nanomaterials and Nanotechnology, Institute of Solid State Physics, Hefei Institutes of Physical Science, Chinese Academy of Sciences, Hefei 230031, People's Republic of China

ARTICLE INFO

ABSTRACT

The controlled chemical conversion of nanomaterials represents an important basis for both understanding the nanoscale chemical activity and exploring new desirable materials. In this work, the region selective ion-exchange transformation of one-dimensional (1D) SnO$_2$ nanotubes (SNT) into three-dimensional (3D) SnS$_2$@SnO$_2$ nanoflowers (SNF) were prepared by combining the electrospinning technique and hydrothermal method. The template-oriented synthesized SnS$_2$@SnO$_2$ demonstrated good dispersibility and uniformity, which can be proved by field-scanning electron microscopy (FE-SEM) and transmission electron microscopy (TEM). Compared with SNT, SNF showed an improved visible light harvest even to the near-infrared light region through Ultraviolet-Visible Spectroscopy (UV–vis). What's more, SNF showed enhanced water purification performance for oxalic acid-induced photocatalytic reduction of Cr(VI) under visible light irradiation at room temperature, which could be attributed to the staggered band alignment formed between the two semiconductors. Besides, the corresponding mechanism of enhanced photocatalysis regarding the separation of the photogenerated electron-hole pairs for the heterojunction has also been investigated through photoluminescence spectroscopy (PL) and photocurrent analysis.

1. Introduction

Nowadays, water pollution caused by heavy metal ions has drawn extensive attention; among the heavy metals, Cr(VI) is particularly hazardous owing to its acute toxicity to humans and its high mobility in water. Various techniques have been used to treat Cr(VI) contamination, including ion exchange, electrocoagulation, membrane separation, adsorption, and photocatalytic reduction. Among these methods, ion exchange and membrane separation methods are not attractive because of their high operating costs, complicated procedures and harsh conditions. Electrocoagulation and adsorption methods are only able to transfer Cr(VI) but not effectively degrade its toxicity; these must be followed by secondary treatments. Semiconductor-mediated photocatalytic reduction (TiO$_2$, SnO$_2$ etc.) has been proposed as an economical and efficient method for the removal of Cr(VI), especially when it present in low concentration.

However, the natural wide bandgap (Eg = 3.56–3.66) [1,2] limits the application of SnO$_2$ nanomaterials which could only harvest light in ultraviolet region and are not responsive to the visible light (>420 nm) that accounts for about 46% of the whole solar energy [3]. Moreover, high recombination ratio of photoinduced electron hole pairs also restricts their practical photocatalytic performance. Coupling with semiconductors with narrower bandgap to form a construction of heterojunctions has been proved to be an effective way to widen response range to solar energy and improve photocatalytic efficiency. The semiconducting metal sulfides (CdS, SnS$_2$ etc.) are good materials to harvest light in the visible and short-wavelength near-infrared regions, which enables them a promising class of visible light-driven photocatalysts or sensitizers for wide bandgap semiconductors [4–6]. Among them, CdS with a band gap

* Corresponding author. Tel.: +86 37167739533.
** Corresponding author.
E-mail addresses: Zhangp@zzu.edu.cn (P. Zhang), Hujh@zzu.edu.cn (J. Hu).

of 2.4 eV, attracted most significant attention because of its excellent light harvest ability under visible light [7–9]. However, due to its natural acute toxic, CdS is highly pernicious to human health and environment. Among the semiconducting metal sulfides remaining, tin disulfide (SnS$_2$) has caught considerable attention. SnS$_2$ is a CdI$_2$-type layered semiconductor with a band gap of 2.2–2.25 eV [10,11]. SnS$_2$ is nonpoisonous, relatively inexpensive, chemically stable in acid or neutral aqueous solution, and has been proved to be an efficient visible-light-driven photocatalyst [12,13]. Moreover, it has been demonstrated that SnS$_2$ has matched band potentials with SnO$_2$ to form well-suited heterojunction [14].

In the very limited studies undertaken hitherto, SnS$_2$/SnO$_2$ composites have demonstrated great potential in achieving higher visible-light-driven photocatalytic. And, the existing synthesis methods of SnS$_2$/SnO$_2$ composite photocatalysts involved multi-steps or toxic and expensive organic solvents, which is hard to control to arrive at monodisperse heterojunction with well-designed structure and morphology. Therefore, it is highly challenging but desirable to develop a direct effective approach to control their composition, morphology and crystal phase. Among various approaches, the ion-exchange reaction of nanostructures has been attracting intense attention because it enables the efficient chemical transformation from one crystalline material to another with adjustable composition and controlled crystal phase. And, the starting templates are usually important to define the morphology, dimension and size of the heterojunction composites. Inspired by our previous work [15,16], electrospun SnO$_2$ nanotubes are actually composed of uniform SnO$_2$ nanoparticles interacted with each other along 1D direction, which made it possible to benefit the conversion from 1D nano-templates into 3D nanostructures via the ion-exchange strategy.

Herein, we reported a successful attempt for the fabrication of mono-dispersed SnS$_2$@SnO$_2$ hetero-nanoflowers by combining the single capillary electrospinning technique and hydrothermal method. The template-oriented method demonstrated good dispersibility and uniformity, which can be proved by field-scanning electron microscopy (FE-SEM) and transmission electron microscopy (TEM). What's more, SNF showed enhanced water purification performance for oxalic acid-induced photocatalytic reduction of Cr(VI) under visible light irradiation at room temperature, which could be attributed to the staggered band alignment formed between the two materials. Besides, the corresponding mechanism of enhanced photocatalysis regarding the separation of the photogenerated electron-hole pairs for the heterojunction has also been investigated through photoluminescence spectroscopy (PL) and photocurrent analysis.

2. Experimental

2.1. Fabrication of SnO$_2$ nanotubes (SNT)

In a typical procedure for fabrication of SnO$_2$ nanotubes, a precursor was primarily prepared before electrospinning process. First, 0.225 g tin dichloride dehydrate (SnCl$_2$·2H$_2$O, Tianjin Chemical Corp., China) was dissolved into a solvent blend which contained 2.2 g ethanol (99.9%) and 2.2 g N, N-dimethylformamide (DMF, >99.5%, Shanghai Chemical Reagent Company) at room temperature with strong stirring. 0.4 g polyvinyl pyrrolidone (PVP, Sigma-Aldrich, Mw = 1,300,000 g mol^{-1}) was afterwards added to the above solution and stirred for another 6 h to form the homogeneous precursor. Then, the precursor solution was transferred into a 5 ml plastic syringe and the feeding rate was adjusted to 0.3 ml h^{-1} using a suitable stainless steel needle, which was connected to a direct-current power supply. A piece of aluminium foil was uesd as a collector and placed 15 cm below the tip of the needle. When

the high voltage of 20 kV was applied, white nanofibers were fabricated and deposited on the aluminium foil. To crystallize SnO$_2$ and remove the polymer, as-spun nanofibers were calcined at 600 °C in air for 3 h in a muffle furnace with the heating rate of 2 °C min^{-1}, and hollow SnO$_2$ nanotubes were obtained.

2.2. Preparation of SnS$_2$@SnO$_2$ nanoflowers

SnS$_2$@SnO$_2$ nanoflowers were prepared by hydrothermal method based on the SnO$_2$ nanotubes. Firstly, 0.01 mol thioacetamide (TAA, Tianjin Chemical Corp., China), 2 ml glacial acetic acid (99.5%, Sinopharm Chemical Reagent Beijing Co., Ltd) and 38 ml deionized water were put into a Teflon-lined stainless steel autoclave of 100 ml capacity under strong stirring to form a homogeneous solution. Then 0.0015 mol SnO$_2$ nanotubes were added. After vigorous stirring for 20 min, two identical autoclaves were sealed and heated in different electric ovens at 150 °C for different time, and then cooled to room temperature naturally. The suspensions were collected by filtration, and the products were washed with deionized water for several times and dried in oven at 80 °C for 4 h.

For the convenience of description, the SnS$_2$@SnO$_2$ nanoflowers obtained under different conditions were named as "SNTF" and "SNF" corresponding to the samples heated for 3 h and 6 h, respectively.

2.3. Characterization

The morphologies of as-obtained nanomaterials were observed using field emission scanning electron microscopy (FESEM; JSM-7500F) and transmission electron microscopy (TEM; FEI Tecnai G2 F20). The structure and phase composition were investigated from 10° to 70° at a scanning rate of 4°/min by powder X-ray diffraction (XRD) on a D/max 2500 XRD diffractometer (Rigaku) with CuKα radiation (λ = 0.1541 nm) under a voltage of 40 kV and a current of 30 mA. Resonant Raman spectra analysis were made on a Jobin-Yvon HR800 micro-Raman spectrometer using a 532 nm line of a He–Cd laser as the excitation source at room temperature. X-ray photoelectron spectroscopy (XPS) of the samples was conducted on an ESCALAB 250 spectrometer (Thermo Scientific Ltd., England) with Al Ka (1486.6 eV) as radiation source. The photoluminescent (PL) performance was tested with a Jobin Yvon HR800 micro-Raman spectrometer using a 325 nm line laser. UV–vis (UV–vis) diffuse reflectance tests were carried out on a Shimadzu UV3600 spectrophotometer equipped with an integrating sphere in the range of 200–800 nm and standard BaSO$_4$ powder was used as a reference.

2.4. Photoelectrochemical experiment

Photoelectrochemical measurements were performed using a conventional three-electrode setup on an electrochemical workstation (AMETEK, PARSTAT 4000, America). The setup had pure SnO$_2$/FTO and SnS$_2$@SnO$_2$/FTO as working electrodes, and a Pt wire and an Ag/AgCl (saturated KCl) electrode were used as the counter electrode and reference electrode, respectively. All the samples were mixed with 0.05 g polyethylene glycol and 0.35 ml deionized water followed by being casted on the FTO conducting glass. The assembled photoanode was covered by a piece of transparent glass to avoid the samples fall off. Effective area of single photoanode was 1.5 × 1.5 cm^2. The electrolyte was 0.2 M Na$_2$SO$_4$ aqueous solution. A 300 W xenon lamp (Beijing Perfectlight Co., Ltd) with a cutoff filter (λ > 420 nm) was used as the visible light source. The photocurrent response spectroscopy measurement was carried out at a constant potential of +0.9 V to the working photoanode. Electrochemical impedance spectra (EIS) were measured at an open-circuit voltage.

A sinusoidal ac perturbation of 5 mV was applied to the electrode over the frequency range of 100 mHz to 10 kHz.

2.5. Photocatalytic activity evaluation

Measurement of the photocatalytic activity was performed by the dichromate reduction in an aqueous solution at room temperature. A 150–350 W xenon lamp was used as a visible light source, which irradiated through a cut-off filter (λ > 420 nm, Shanghai Lansheng Sci-tech Co., Ltd., China) onto the reactor. For each test, 20 mg sample was added into 60 ml 2×10^{-4} M dichromate solution. The solution was first stirred under the dark condition for 2 h to reach adsorption−desorption equilibrium and then transferred into a sealed reactor. At given time intervals, 5 ml of each sample were removed from the reactor, which were then centrifuged to separate the catalyst particles. The reduction of the Cr(VI) solution was determined by measuring the maximum light absorbance of filtrates using a UV–vis spectrophotometer (Shimadzu-UV3600, Japan). The reduction percentage of the Cr(VI) solution was calculated using Rate $= C/C_o = A_t/A_o$, Where A_o is the absorbance of the fresh dichromate solution and A_t is the absorbance of the dichromate solution after a given irradiation period.

3. Results and discussion

3.1. The morphologies of the as-prepared nanomaterials

$SnS_2@SnO_2$ hetero-nanoflowers were obtained via an ion exchange sulfide process from SnO_2 nanotube which was prepared by electrospinning (Scheme 1). Inspired by our previous work [15], electrospun SnO_2 nanotubes are actually composed of uniform SnO_2 nanoparticles interacted with each other along 1D direction. During the ion exchange process at 150 °C, the surface of the SnO_2 nanotube firstly being vulcanizing by the added thioacetamide in the acidic conditions, and it is supposed that the SnS_2 was formed
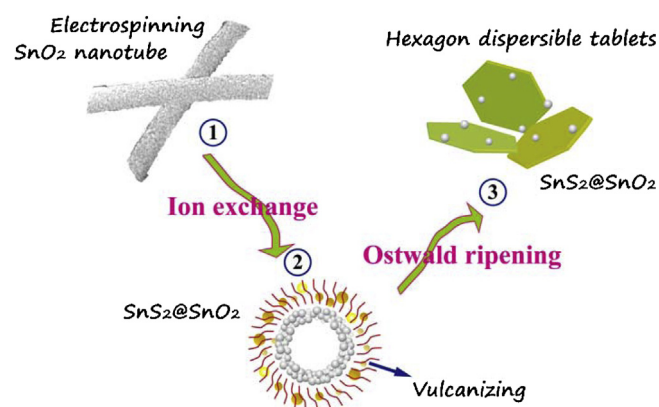
Scheme 1. Schematic diagram of the synthesis of $SnS_2@SnO_2$ hetero-nanoflowers from SnO_2 nanotube via electrospinning and vulcanizing process.

due to the sulfur ion replacing the oxygen ion in the SnO_2. After that, the ostwald ripening led to the formatting of $SnS_2@SnO_2$ hierarchical structure [16,17]. The SnO_2 nano tubes provided mass transfer channels for sulfur ions and template for formation a coalesced hetero structure of residual $SnO2$ and $SnS2$. which made it possible to benefit the conversion from 1D nano-templates into 3D nanostructures via the ion-exchange strategy. The resultant dispersive and uniform $SnS_2@SnO_2$ hetero-nanoflowers were with a size of several hundred nanometers. The morphologies of as-prepared nanomaterials were observed by field-emission scanning electron microscopy (FESEM) and transmission electron microscopy (TEM). The SnO_2 material obtained by electrospinning technique exhibited fine free-standing one-dimensional tubular nanostructure with a diameter of about 200 nm (see Fig. 1A and B). After 6 h hydrothermal treatments in thioacetamide acid-deficient solution at 150 °C, it could be seen from Fig. 1C that the samples grew into uniform flower-like spheres which were well separated and were in an aver-
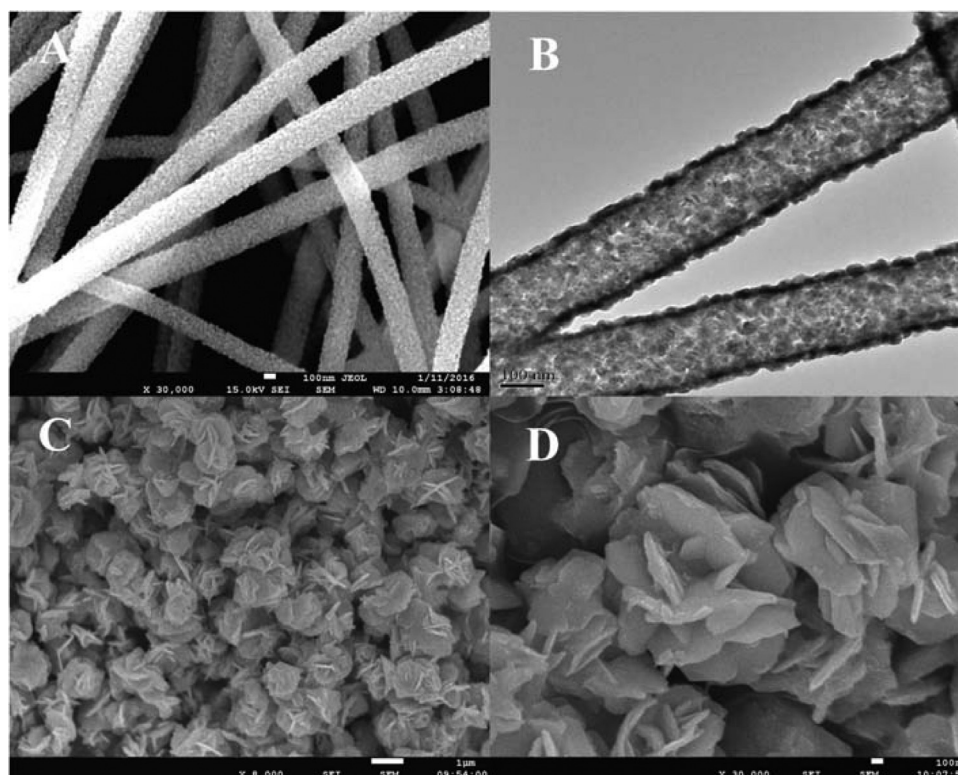
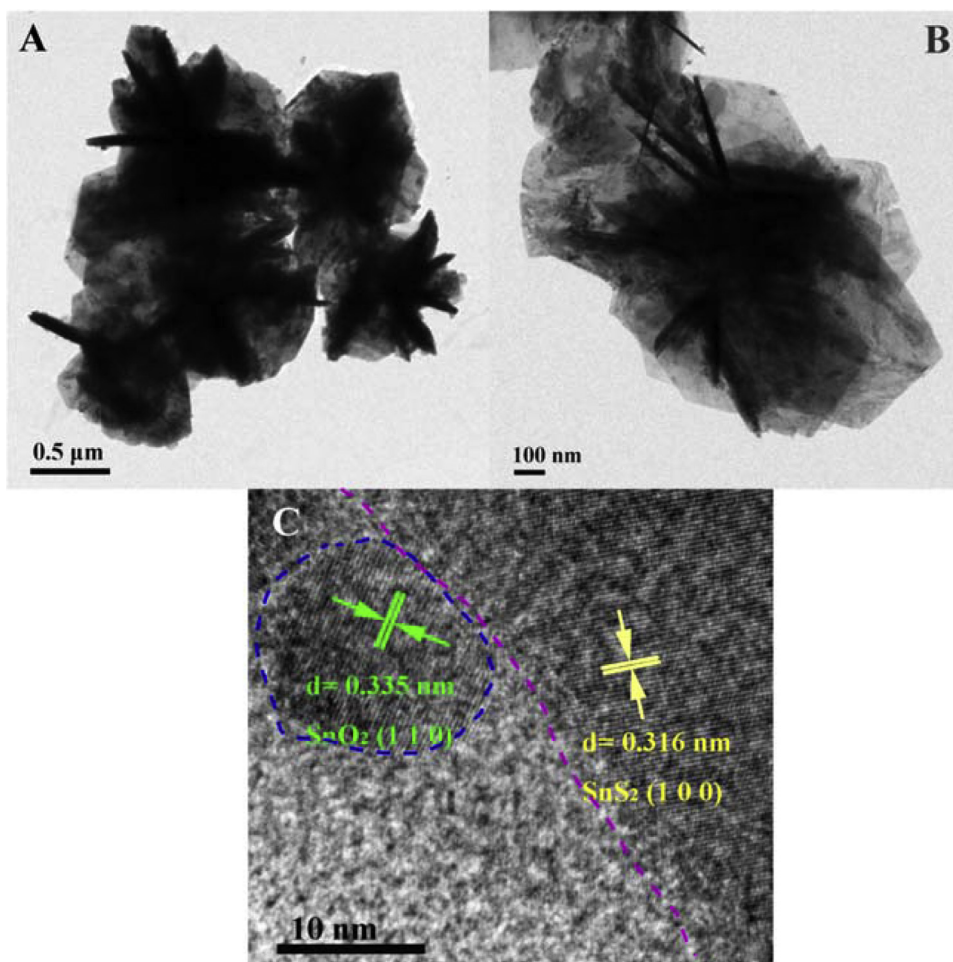**Fig. 1.** FESEM/TEM images of the $SnS_2@SnO_2$ hetero-nanoflowers.

Fig. 2. TEM images (A and B) and HRTEM image (C) of as-prepared $SnS_2@SnO_2$ hetero-nanoflowers.

age diameter of 1 μm. Additionally, the enlarged view of the hybrid material were futher displayed in Fig. 1D, it could be observed that individual sphere was composed of intersected nanoflakes in nearly hexagon, the thickness of which were about 10 nm. The large surface area of nanoflakes oriented by tubular templates from SNT, were likely to help serve more active sites for chemical reactions.

3.2. TEM of the as-prepared composite nanoflowers

Transmission electron microscopy (TEM) and high-resolution transmission electron microscopy (HRTEM) were further carried out to show microstructure of flakes on flower-like spheres in details (Fig. 2A). It was obvious that the nanoflakes were intersected with each other to form the flower-like construction. HRTEM image in Fig. 2C reveals that the interplanar spacings of the lattice fringes are 0.335 nm and 0.316 nm, respectively, which are well corresponding to the (1 1 0) planes of tetragonal phase SnO_2 and (1 0 0) planes of hexagonal phase SnS_2 respectively[18]. Thus, the formation of $SnS_2@SnO_2$ hetero structure was confirmed.

3.3. X-ray diffraction (XRD) patterns

Fig. 3 shows the typical powder XRD patterns of pure SnO_2 nanotubes and $SnS_2@SnO_2$ nanoflowers. There were nine diffraction peaks in curve D in Fig. 3, which were finely attributed to the tetragonal rutile SnO_2 structure (space group P42/mnm, $a_0 = b_0 = 4.737$ Å, $c_0 = 3.186$ Å, JCPDS, No. 88-0287). Besides, no extra diffraction peaks attributed to Sn and SnO secondary phases were observed in curve

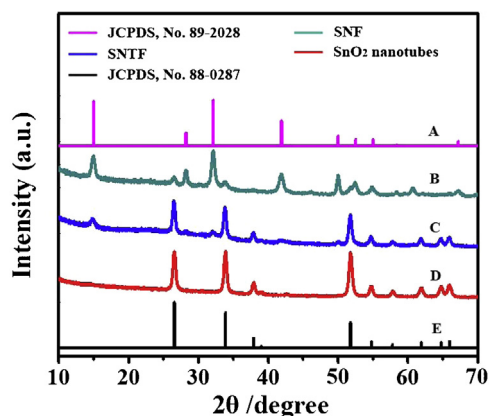**Fig. 3.** XRD patterns of as-prepared (B) SNF, (C) SNTF and (D) SnO_2 nanotubes.

D, implying a relatively high purity of SnO_2 nanotubes obtained by electrospinning technique. The sharp and intense diffraction peaks further indicated the good crystallinity of tetragonal SnO_2. After pure SnO_2 nanotubes were vulcanized at 150 °C for 3 h, weak peaks appeared in the composite SNTF at $2\theta = 15.03°$ (0 0 1), 28.25° (1 0 0), 32.14° (1 0 1), 41.92° (1 0 2) in curve C [19,20], which were indexed to hexagonal SnS_2 phase (space group P-3m1 (164), $a_0 = b_0 = 3.6450$ Å, $c_0 = 5.8910$ Å, JCPDS, No. 89-2028). When the heating time of hydrothermal treatment was extended to 6 h, the diffraction peaks of SnS_2 became more evident and much sharper,
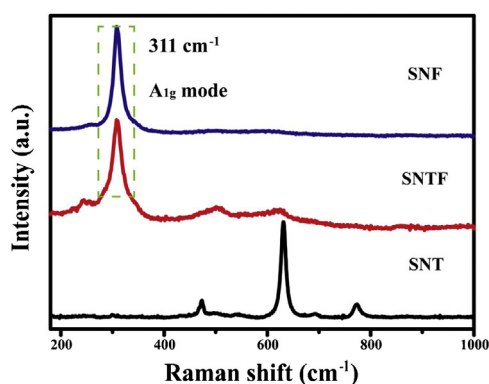
Fig. 4. Raman spectra of as-prepared nanomaterials.

giving a hint about the improvement in the crystallinity and content of SnS$_2$ in the composite.

3.4. Raman spectra

Fig. 4 exhibits the Raman spectra of as-prepared SnO$_2$ nanotubes (SNT), SNTF and SNF with the employment of high resolution co-focus Raman spectroscopy, a more surface-sensitive technique for the evaluation of chemical state of inorganic materials. As Fig. 4 shows, three characteristic vibration peaks were observed in pure SnO$_2$ nanotubes. The strong peak at 633 cm^{-1} belongs to the A$_g$ vibration model of SnO$_2$ nanomaterials [21], and weak peaks at 475 cm^{-1} and 777 cm^{-1} belong to E$_g$ and B$_{2g}$ vibration model of

SnO$_2$, respectively. After pure SnO$_2$ nanotubes being vulcanized by thioacetamide acid-deficient solutions, these above peaks became weaker and disperaed compleltely, in SNF. The strong characteristic vibration peaks appeared in SNTF and SNF at 311 cm^{-1}, which were assigned to the A$_g$ vibration model of SnS$_2$ materials [22,23]. The appearance of new peak of SnS$_2$ further confirmed the heterostructure between SnS$_2$ and SnO$_2$.

3.5. XPS spectra of the as-prepared composite SNF

The chemical states of Sn, S and O were further accessed by XPS and the representative spectra are shown with the as-prepared SNF undergone 6 h hydrothermal treatment. As shown in Fig. 5A, the XPS survey spectra displayed the presence of Sn, S, O and C in SNF without any other peaks of impurity or byproduct, while C1s was used as a reference to calibrate spectra. Fig. 5B showed the presence of sharp peaks at 486.5 eV and 494.9 eV, which can be attributed to the binding energies of Sn 3d$_{5/2}$ and Sn 3d$_{3/2}$ [24], respectively, and their splitting between them was just 8.4 eV which suggesting the existence of valence state of Sn^{4+} in SNF. The high-resolution XPS spectrum of S 2p core level analysis (Fig. 5C) displayed the presence of peak at 160.8 eV for divalent sulfide ions (S^{2-}) in SnS$_2$. In addition, the binding energy of O 1s in SNF was observed at about 532.7 eV from Fig. 5D, in accordance with the literature reports [25–27]. The XPS study is well consistent with the Raman and XRD analysis.

3.6. UV–vis diffuse reflectance spectra

Fig. 6 shows the UV–vis diffuse reflectance (DR) spectra of as-prepared SnS$_2$@SnO$_2$ hetero-nanoflowers and pure SnO$_2$ nano-
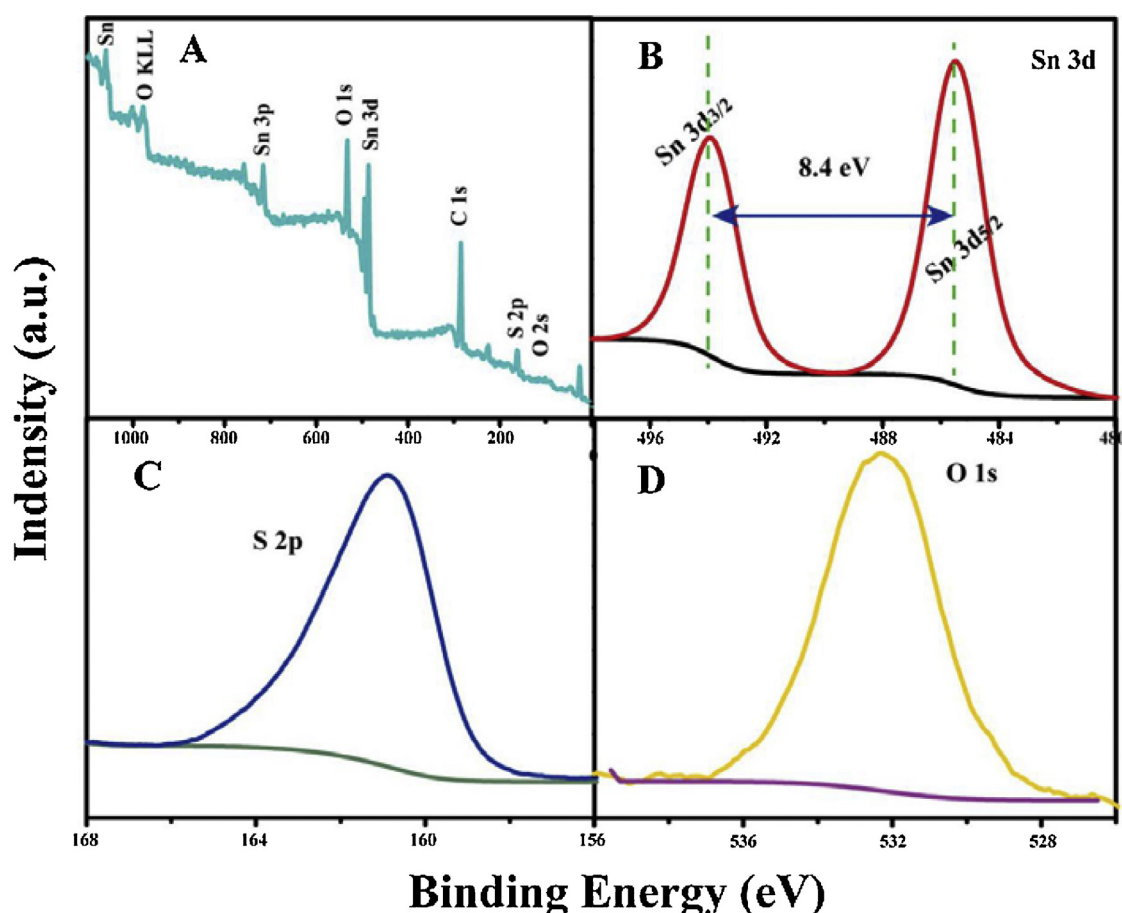

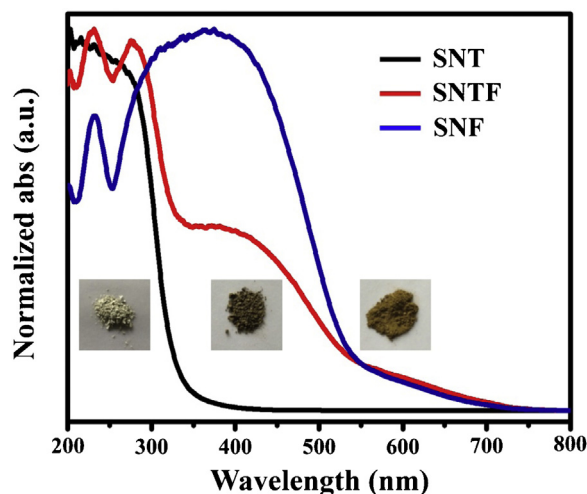**Fig. 5.** (A) XPS spectra and (B, C and D) high-resolution XPS spectra of Sn 3d, S 2p, O 1s in SNF.

Fig. 6. DR spectra of as-prepared SnO_2 nanotubes, SNTF and SNF.

tubes. As observed, pure SnO_2 nanotubes displayed typical DR spectrum of tetragonal rutile SnO_2 with a cut-off wavelength at ~350 nm, in correspondence to its wide band gap of 3.6 eV [1,2]. Notably, broader visible-light absorption at 350–800 nm can be seen in all $SnS_2@SnO_2$ nanoflowers, indicating that the biphase $SnS_2@SnO_2$ are of great promise to be efficient visible-light-driven photocatalysts. The reason for the absorption of visible light could be attributed two parts: one was from the SnS_2 itself, the band gap of which was only 2.4 eV, could absorb visible light; the other was a joint electronic system formed between SnO_2 and SnS_2, which gave rise in synergistic properties. It could be explained by the energy level matching prinpicle. Based on relative energy level, the conduction band (CB) of SnS_2 was higher than the CB of SnO_2 and the value band (VB) of SnS_2 was lower than the VB of SnO_2. When SnS_2 was induced by visible light, photogenerated electron would transfer from the CB of SnS_2 to the CB of SnO_2, while photogenerated holes remained in the VB of SnS_2. In addition, it could be seen that the visible light harvest of SNF was higher than that of SNTF, which was likely due to the higher content of SnS_2 in SNF.

3.7. Photoluminescence (PL) spectra and incident photon-to-electron conversion (IPCE) spectrum

To address the effect of $SnS_2@SnO_2$ heterojunctions on electron-hole separation indirectly, photoluminescence spectra (PL spectra) was employed to characterize the recombination probability in pure SnO_2 nanotubes and $SnS_2@SnO_2$ hetero-nanoflowers. PL spectra in the wavelength of 350–650 nm are displayed in Fig. 7. No obvious emission peak can be found around 400 nm, indicating that these PL signals did not result directly from the electron transition from the conduction band to valence band. All of these samples showed similar curves with one emission peak located at 503 nm. The PL intensities of $SnS_2@SnO_2$ nanoflowers were lower than that of SnO_2 nanotubes, implying lower electron–hole recombination probability in $SnS_2@SnO_2$ hetero-nanoflowers [28]. Combined with the UV–vis diffuse reflectance spectra, the PL spectra have further confirmed the good formation of heterojunctions between SnS_2 and SnO_2. Electrons and holes are separated by the heterojunctions in electric field between SnS_2 and SnO_2, leading to a decrease of PL intensity in $SnS_2@SnO_2$ nanoflowers. What is more, the SNF sample showed the lowest PL intensity, suggesting its highest electron–hole separation efficiency. Compared with PL spectra, the incident photon-to-electron conversion (IPCE) spectrum is powerful to quantitatively reveal their photocatalytic activity as a function of wavelength of incident light, which is
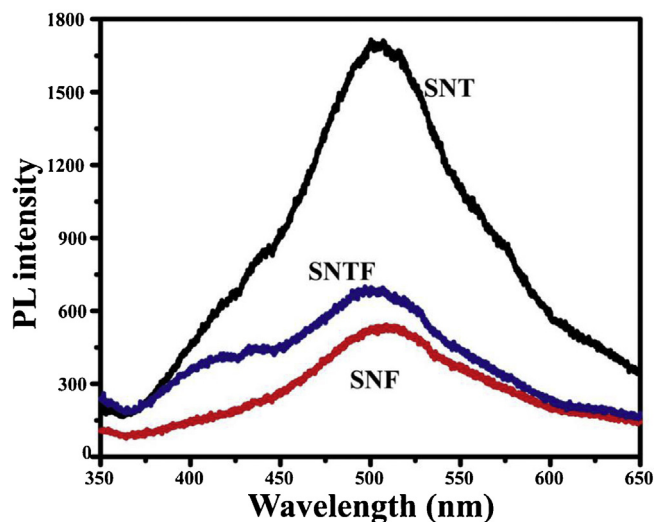

Fig. 7. Photoluminescence spectra of as-prepared samples with excitation wavelength: ca. 325 nm.

important to confirm the increased photocatalytic activity. The spectra of the incident photon-to-current conversion efficiencies (IPCE) of the samples was test using a power source (Newport 300W xenon lamp, 66920) with a monochromator (Newport Cornerstone 260) and a multimater (Keithley 2001). As the spectra of incident photon-to-current conversion efficiencies exhibited(shown in Fig.S1), in identical situation, three different samples showed the same IPCE peak at around 350 nm and compared with SNF electrode, an obvious improvement on IPCE was observed in SNTF electrode and SNF electrode under both UV and visible light. The IPCE peak of SNT electrode at 350 nm was 1.2%, while the IPCE peak of SNTF electrode and SNF electrode were 1.73% and 2.07% respectively. In the wavelength of 400–600 nm, no free electron was received in SnO_2 nanotubes electrode, by contrast, $SnS_2@SnO_2$ nanoflowers displayed obviously enhanced response in visible light, which clearly illuminated that the heterojunction between SnS_2 and SnO_2 could help retard the hole-electron recombination process through interfacial charge transfer. These results further demonstrated that the improved Cr(VI) photoreduction by $SnS_2@SnO_2$ hetero-nanoflowers was induced by increased valid photogenerated electron.

3.8. Photocatalytic activity

The photocatalytic activities of as-prepared $SnS_2@SnO_2$ hetero-nanoflowers were estimated by detecting the photocurrents and the degradation rate of toxic aqueous Cr(VI) under visible light irradiation. The photocurrents were tested for SNT, SNTF and SNF with 0.2 M Na_2SO_4 solution as electrolyte with full spectrum light irradiation and visible light irradiation, separately (Fig. 8A and B). As shown in Fig. 8A and B, it was clear that fast and uniform photocurrent responses were observed in all electrodes and the photoresponsive phenomenon was reversible.

Under full spectrum light irradiation, the photocurrent of SNF electrode was about five times as high as that of SNT, and more than two times higher than that of SNTF electrode. When the cut-off filter ($\lambda > 420$ nm) was applied, SnO_2 nanotubes also showed little photocurrent response to visible light (Fig. 9B). In contrast, SNF electrode demonstrated a noticeable photocurrent response under visible light irradiation. The inset image in Fig. 8B was the enlarged curves from range 200–500 s, and we can see it has three stages which were corresponding to the full spectrum, visible light and shading (The test were repeated by identical time interval).
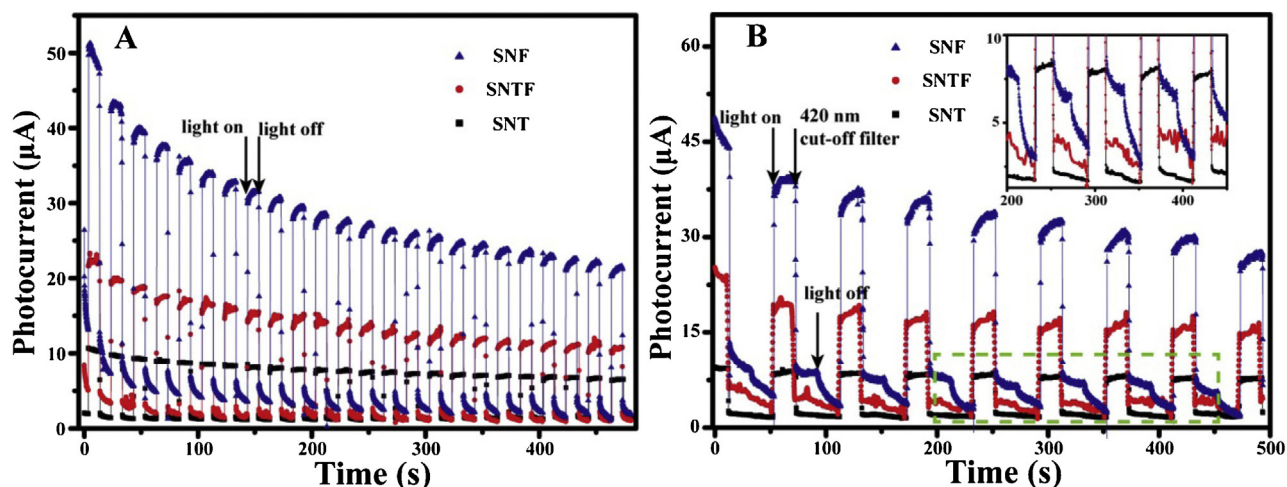
Fig. 8. (A) Photocurrents of SNT, SNTF and SNF electrodes under full spectrum light irradiation and (B) under full spectrum and visible irradiation ($\lambda > 420$ nm) ([Na_2SO_4]$^-$ 0.2 M).
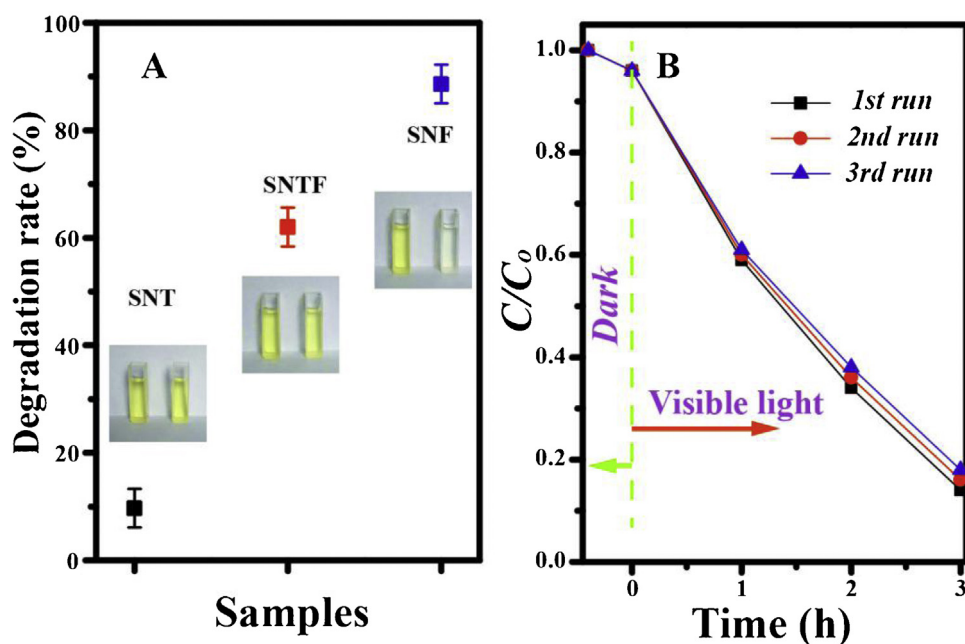

Fig. 9. (A) Photocatalytic activities of SNT, SNTF and SNF in the reduction of 80 ml of 5×10^{-4} M Cr(VI) under visible light ($\lambda > 420$ nm) irradiation (Note: the dosage of photocatalyst is 20 mg); (B) Photocatalytic performance of SNF with three times of cycling uses.

The photocurrent improvement both under full spectrum light and visible light irradiation of SNF and SNTF photocatalyst suggested an enhancement of photogenerated electrons and holes separation, which could be owing to the extended visible light absorption and irreversible electrons transfer across SnS_2-SnO_2 heterojunction.

In order to further assess the photocatalytic performance of as-prepared $SnS_2@SnO_2$ composite nanoflowers, aqueous Cr(VI) was chosen to be degraded under 300W xenon lamp irradiation, which is widely used in electroplating, leather tanning and dyeing, highly toxic to environment as well as human health, especially to human liver, kidney and skin. Fig. 9A showed the photocatalytic activities of SNT, SNTF and SNF in the reduction of aqueous Cr(VI) under visible light ($\lambda > 420$ nm) irradiation within the same treatment time. As can be seen from Fig. 9A, SnO_2 nanotubes showed a slight visible-light-driven photocatalytic activity. Nevertheless, SNTF and SNF photocatalysts both exhibited considerably high photocatalytic activities in the reduction of aqueous Cr(VI) under visible

light ($\lambda > 420$ nm) irradiation. More importantly, SNF photocatalyst displayed the highest photocatalytic activity, which could achieve a nearly 90% degradation rate under visible light ($\lambda > 420$ nm) irradiation.

In addition, the cycling reuse ability with continuously high photocatalytic activity was another critical issue for long-term use in practical applications. Herein, to investigate the stability of the SNF photocatalyst, SNF photocatalyst was reused for three times under identical conditions. It could be observed from Fig. 9B that the photocatalytic activity of SNF catalyst remained almost unchanged in recycling reactions. And in this work, the unique nanoflower morphology of SNF photocatalyst could be easily separated from aqueous solutions by sedimentation. Thus, it demonstrated that SNF photocatalyst demonstrated an efficient photoactivity for the reduction of toxic aqueous Cr(VI) and could be effectively reused in high efficiency.
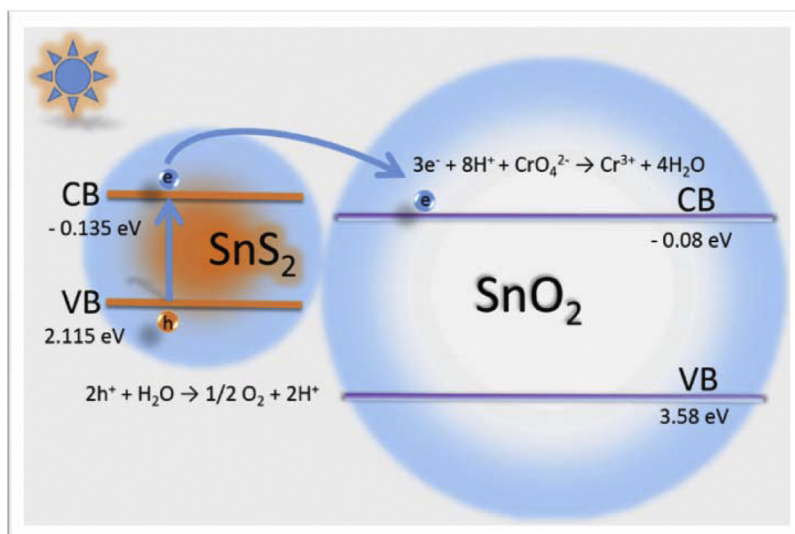
Scheme 2. Postulated mechanism of visible light-induced photoreduction of Cr^{6+} with the $SnS_2@SnO_2$ nanocomposites.

3.9. Photocatalytic action mechanism

On the basis of the current experimental results, possible mechanisms for UV and visible light photocatalysis are elucidated schematically in Scheme 2. Via Mulliken electronegativity theory: $EVB = X_{semiconductor} - E_0 + 0.5E_g, 0.5E_g$, where EVB is the VB edge potential, $X_{semiconductor}$ is the electronegativity of the semiconductor, which is the geometric mean of the electronegativity of the constituent atoms, E_0 is the standard electrode potential on the hydrogen scale (ca. 4.5 eV). E_g was derived from $Eg = 1239.8/\lambda g$, where λg is the absorption edge in the UV–vis spectra (shown below). So far, considerable success had been achieved in predicting the relative band edge positions for many oxide and sulfide semiconductors using this method. In our case, the calculated results were E_{CB} (SnS_2) = −0.135 eV, E_{VB} (SnS_2) = 2.115 eV and E_{CB} (SnS_2) = −0.08 eV, E_{VB} (SnS_2) = 3.58 eV [29,30]. Although these data may not be the exact absolute values for the CB and VB potentials of SnS_2 and SnO_2, they would offer a reliable estimation of the relative band edge positions of the two semiconductors. Thus, a schematic diagram of the energy band structures of SnS_2/SnO_2 composite is illustrated in Scheme 2, which is similar to that of the well-studied CdS/TiO_2. When the SnS_2/SnO_2 nanocomposites were irradiated by visible light ($\lambda > 420$ nm), SnO_2 had no response ability due to its wide band gap ($Eg = 3.66$ eV), but the electrons in the VB of $\Box SnS_2$ can be excited to its CB with simultaneous generation of the same amount of holes in its VB. The CB of SnO_2 was more positive than that of SnS_2, resulting in a local electric field. As a result, the excited electrons can readily transfer from the CB of $\Box SnS_2$ to the CB of SnO_2 via interface, whereas the generated holes still remained on the VB of SnS_2. In this way, the photoinduced charge carriers in SnS_2 nanoparticles can be effectively separated, and accordingly their recombination was suppressed. The efficient charge separation can increase the lifetime of the charge carriers and enhance the efficiency of the interfacial charge transfer to adsorbed substrates. The separated electrons undertake the one-electron reduction reaction of Cr(VI) to generate Cr(III). The proposed reaction pathway for the photocatalytic reduction of Cr(VI) under visible light is as follows:

$$2\,h^+ + H_2O \rightarrow 1/2O_2 + 2H^+ \tag{1}$$

$$3e^- + 8H^+ + CrO_4^{2-} \rightarrow Cr^{3+} + 4H_2O \tag{2}$$
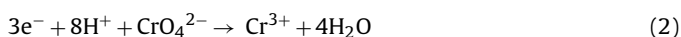
So, it is reasonable that the SnS_2/SnO_2 nanocomposites could demonstrate excellent photocatalytic efficiency.

4. Conclusions

We reported a successful attempt for the fabrication of monodispersed $SnS_2@SnO_2$ hetero-nanoflowers by combining the single capillary electrospinning technique and hydrothermal method. The template-oriented method demonstrated good dispersibility and uniformity, which can be proved by field-scanning electron microscopy (FE-SEM) and transmission electron microscopy (TEM). What's more, SNF showed enhanced water purification performance for oxalic acid-induced photocatalytic reduction of Cr(VI) under visible light irradiation at room temperature, which could be attributed to the staggered band alignment formed between the two structures. Besides, the corresponding mechanism of enhanced photocatalysis regarding the separation of the photogenerated electron-hole pairs for the heterojunction has also been investigated through photoluminescence spectroscopy (PL) and photocurrent analysis.

Appendix A. Supplementary data

Supplementary data associated with this article can be found, in the online version, at http://dx.doi.org/10.1016/j.apcatb.2016.03.035.

References

[1] Y.C. Zhang, Z.N. Du, M. Zhang, Mater. Lett. 65 (2011) 2891–2894.
[2] X. Zhou, T. Zhou, J. Hu, J. Li, Cryst. Eng. Commun. 14 (2012) 5627–5633.
[3] L.J. Wang, J.J. Fan, Z. Cao, Y.C. Zheng, Z.Q. Yao, G.S. Shao, J.H. Hu, Chem. Asian J. 9 (2014) 1904–1912.
[4] Y. Xie, G. Ali, S.H. Yoo, S.O. Cho, ACS Appl. Mater. Interfaces 2 (2010) 2910–2914.
[5] M. Basu, A.K. Sinha, M. Pradhan, S. Sarkar, Y. Negishi, T. Pal, Environ. Sci. Technol. 44 (2010) 6313–6318.

[6] A.H. Zyoud, N. Zaatar, I. Saadeddin, C. Ali, D. Park, G. Campet, H.S. Hilal, J Hazard. Mater. 173 (2010) 318–325.
[7] Y. Tak, H. Kim, D. Lee, K. Yong, Chem. Commun. 38 (2008) 4585–4587.
[8] S. Xiong, B. Xi, Y.J. Qian, Phys. Chem. C 114 (2010) 14029–14035.
[9] Y. Guo, L. Wang, L. Yang, J. Zhang, L. Jiang, X. Ma, Mater. Lett. 65 (2011) 486–489.
[10] X. Li, J. Zhu, H. Li, Appl. Catal. B 123–124 (2012) 174–181.
[11] E. Ramasamy, J. Lee, J. Phys. Chem. C 114 (2010) 22032–22037.
[12] H.Y. He, J.F. Huang, L.Y. Cao, J.P. Wu, Z. He, L.J. Luo, Adv. Mater. 9 (2007) 3781–3784.
[13] J.H. Liu, G.F. Huang, W.Q. Huang, H. Miao, B.X. Zhou, Mater. Lett. 161 (2015) 480–483.
[14] Y.C. Zhang, Z.N. Du, K.W. Li, M. Zhang, D.D. Dionysiou, ACS Appl. Mater. Interfaces 3 (2011) 1528–1537.
[15] P. Zhang, L.J. Wang, X. Zhang, J.H. Hu, G.S. Shao, Nano-Micro Lett. 7 (2015) 86–95.
[16] Peng Zhang, Lijie Wang, Xi Zhang, Changlu Shao, Junhua Hu, Guosheng Shao Appl. Catal. B: Environ. 166 (2015) 193–201.
[17] D.V. Alexandrov, J. Phys. Chem. Solids 91 (2016) 48–54.
[18] Y.C. Zhang, Z.N. Du, S.Y. Li, M. Zhang, Appl. Catal. B 95 (2010) 153–159.
[19] Q.R. Zhao, Y. Gao, X. Bai, C. Wu, Y. Xie, Eur. J. Inorg. Chem. 8 (2006) 1643–1648.
[20] H.L. Tang, X. Qi, W.J. Han, L. Ren, Y.D. Liu, X.Y. Wang, J.X. Zhong, Appl. Surf. Sci. 355 (2015) 7–13.
[21] T. Hirata, K. Ishioka, M. Kitajima, H. Doi, Phys. Rev. B 53 (1996) 844.
[22] M. Liu, J.Y. Yang, Q. Qu, P.W. Zhu, W.X. Li, J. Power Sources 273 (2015) 848–856.
[23] C.Y. Chen, T. Yokoshima, H. Nara, T. Momm, T. Osaka, Electrochim. Acta 183 (2015) 78–84.
[24] X.L. Li, L.B. Chu, Y. Wang, L.S. Pan, Mater. Sci. Eng. B 205 (2016) 46–54.
[25] P. Zhang, C. Shao, Z. Zhang, M. Zhang, J. Mu, Z. Guo, Y. Liu, Nanoscale 3 (2011) 2943–2949.
[26] P. Zhang, C. Shao, Z. Zhang, M. Zhang, J. Mu, Z. Guo, Y. Liu, J. Mater. Chem. 21 (2011) 17746–17753.
[27] C. Wang, C. Shao, X. Zhang, Y. Liu, Inorg. Chem. 48 (2009) 7261–7268.
[28] L. Ma, L.M. Xu, X.Y. Xu, L. Zhang, X.P. Zhou, Ceram. Int. 42 (2016) 5068–5074.
[29] X. Liu, H.L. Zhao, A. Kulka, A. Trenczek-Zajc, J.Y. Xie, N. Chen, Konrad Síwierczek, Acta Mater. 82 (2015) 212–223.
[30] S. Park, J.H. Park, R. Selvaraj, Y. Kim, J. Ind. Eng. Chem. 31 (2015) 269–275.